Spin-Canting Mediated Anomalous Nernst Effect in Ferrimagnetic CoTb Films

Yuheng Li(李宇恒)†, Shi Huang(黄石)†, Wei Zhu(朱伟), Chang Pan(潘昶), Pengwei Gong(宫鹏威), Jianwei Zhang(张建卫)*, and Xuepeng Qiu(丘学鹏)*

School of Physics Science and Engineering, Tongji University, Shanghai 200092, China

(Received 4 December 2025; accepted manuscript online 4 January 2026)

The anomalous Nernst effect (ANE), which enables energy conversion and harvesting in ferromagnetic materials through orthogonal charge generation relative to the heat gradient and magnetization, holds great promise for spintronic thermoelectric applications. However, achieving both perpendicular magnetic anisotropy (PMA) and an out-of-plane thermal gradient—two essential prerequisites for highly stable and efficient spintronic devices—contradicts the orthogonality condition required for ANE generation. In this study, we leverage the novel spin-canting effect in ferrimagnetic CoTb films to realize a pronounced ANE response near the magnetic compensation temperature, yielding a remarkable ANE coefficient of 0.108 μV/K. By further investigating the angular characteristics of the spin-canted state, we optimize and identify the ideal measurement scheme for spin-canting-mediated ANE. Our findings systematically elucidate the unique physical behavior of this unconventional ANE and demonstrate the potential of ferrimagnetic systems with strong PMA for developing high-performance thermoelectric devices.

DOI: 10.1088/0256-307X/43/2/020708 CSTR: 32039.14.0256-307X.43.2.020708

The pursuit of efficient and scalable energy harvesting technologies has spurred significant research in spin-caloritronics, a field that explores the interconversion between heat and spin.[1–5] Among various thermomagnetic effects, the anomalous Nernst effect (ANE) stands out for its ability to generate a transverse electric voltage in ferromagnets under a longitudinal thermal gradient. This phenomenon mainly arises from the collective Berry curvature of the electronic structure or from spin-dependent scattering,[6–10] producing a voltage orthogonal to both the magnetization ($\boldsymbol{M}$) and the applied temperature gradient (∇T), i.e., $\boldsymbol{V}_{\rm ANE} \propto \nabla T \times \boldsymbol{M}$.[11,12] This unique coupling mechanism makes ANE crucial for building simple, two-terminal thermopiles with potential applications in waste-heat harvesting and integrated spintronic sensors. The quest for high-performance ANE-based devices has highlighted two critical material prerequisites: strong perpendicular magnetic anisotropy (PMA) to ensure robust thermal and magnetic stability,[13] and an out-of-plane thermal gradient ($\nabla T \| \hat{\boldsymbol{z}}$) to maximize heat flux integration in thin-film architectures commonly used in microelectronics.

However, a fundamental contradiction emerges when attempting to fulfill these two prerequisites simultaneously for conventional ANE.[7,14] Although a thin film with PMA ($\boldsymbol{M} \| \hat{\boldsymbol{z}}$) and an out-of-plane thermal gradient ($\nabla T \| \hat{\boldsymbol{z}}$) is favorable for device stability, this geometry inherently fails to satisfy the orthogonality condition ($\boldsymbol{M} \perp \nabla T$) necessary for maximizing the ANE response. This inherent limitation has constrained the design and efficiency of PMA-based spintronic thermoelectric devices. Recent efforts to circumvent this issue have explored non-collinear magnetic textures, such as spin spirals and skyrmions,[15–17] where real-space topology can introduce an in-plane magnetization component even in PMA materials. Nonetheless, stabilizing these textures often requires careful materials engineering (e.g., tuning the Dzyaloshinskii–Moriya interaction, magnetic anisotropy, and interfaces) or external control (such as applied magnetic fields, tailored boundary conditions, or strain).[13,18,19] An alternative pathway lies within ferrimagnetic alloys, which contain two anti-parallel coupled magnetic sublattices (e.g., Co and Tb).[20,21] Near their magnetic compensation temperature $T_{\rm M}$, these systems exhibit rich phase transitions, most notably the spin-canting (SC) state.[22–24] When a critical magnetic field is applied, the initially collinear, anti-parallel magnetic sublattices undergo a dramatic, cooperative reorientation into a canted state, breaking the collinearity and creating a non-zero in-plane magnetization component. This SC transition thus provides an alternative route to satisfy the ANE orthogonality condition even in a strong PMA system with the presence of an out-of-plane ∇T.

In this work, we demonstrate a spin-canting mediated anomalous Nernst effect (SC-ANE) in CoTb films, where the magnetic moments of Co and Tb are coupled antiferromagnetically,[25,26] effectively resolving the long-standing orthogonality conflict. Amorphous ferrimagnetic CoTb alloy consists of two antiferromagnetically coupled magnetic sublattices: the transition-metal Co sublattice

†These authors contributed equally to this work.

*Corresponding authors. Email: zhang@tongji.edu.cn; xpqiu@tongji.edu.cn

© 2026 Chinese Physical Society and IOP Publishing Ltd. All rights, including for text and data mining, AI training, and similar technologies, are reserved.

and the rare-earth Tb sublattice. The Co moments are from itinerant 3d electrons, which exhibit relatively weak temperature dependence, whereas the Tb moments are from localized 4f electrons. At a given temperature T, the net magnetization is given by $\boldsymbol{M}(T) = \boldsymbol{M}_{\rm Co}(T) + \boldsymbol{M}_{\rm Tb}(T)$. Near $T_{\rm M}$, each sublattice remains ordered, but the net magnetization becomes zero, i.e., $|\boldsymbol{M}_{\rm Co}(T_{\rm M})| = |\boldsymbol{M}_{\rm Tb}(T_{\rm M})|$.[27] The free energy of the ferrimagnet can be expressed in a two-sublattice mean-field form:

$$\begin{aligned}\mathcal{F} = & -\mu_0 \boldsymbol{H}\cdot(\boldsymbol{M}_{\rm Co}+\boldsymbol{M}_{\rm Tb}) - J_{\rm ex}\boldsymbol{m}_{\rm Co}\cdot\boldsymbol{m}_{\rm Tb} \\ & - K_{\rm eff}(T)(m^2_{{\rm Co},z}+m^2_{{\rm Tb},z}),\end{aligned}$$

where $J_{\rm ex} > 0$ is the antiferromagnetic inter-sublattice exchange constant, and $K_{\rm eff}(T)$ is the effective uniaxial anisotropy. Far from $T_{\rm M}$, the net magnetization is large and the system favors a collinear antiparallel configuration. However, near $T_{\rm M}$, the first term, the Zeeman energy coupled to the small net magnetization, becomes weak, and the collinear state loses stability as the external field increases. Minimization of $\mathcal{F}$ leads the two magnetic moments to deviate from antiparallel alignment along the z-axis, resulting in the onset of an SC state.[28,29]

Thus, we carry out the investigation near the $T_{\rm M}$ of CoTb, where the SC transition is most pronounced. Applying an out-of-plane magnetic field induces the SC state, which in turn generates a clearly measurable ANE voltage with a significant SC-ANE coefficient of up to 0.108 μV/K, highlighting the efficiency of this mechanism. In addition, we systematically investigate the angular dependence of the SC-ANE signal on the applied magnetic field, enabling us to identify and optimize the ideal measurement configuration for maximizing the output.

The film stack was deposited on a 0.5 mm Al_2O_3 substrate using an AJA magnetron sputtering system. The low thermal conductivity of Al_2O_3 allows for the creation of large thermal gradients.[30] The layer structure, from bottom to top, is CoTb (6 nm)/Si_3N_4 (4 nm)/Al_2O_3 (100 nm)/Ta (30 nm), as illustrated in Fig. 1(a). The deposition was carried out under a base pressure below 10^{-7} Torr and an Ar gas flow with the pressure of 3.0 mTorr. The 6 nm-thick CoTb alloy film was deposited by co-sputtering Co and Tb targets with deposition rates of 0.534 nm/s and 0.462 nm/s, respectively. The anomalous Hall effect (AHE) voltage was measured within a Physical Property Measurement System (PPMS), which supplies an out-of-plane magnetic field. Strong PMA of the film stack is confirmed, as shown in Fig. 1(b). When the temperature goes across $T_{\rm M}$, a sign reversal of the AHE voltage is observed. Irrespective of whether Co or Tb dominates the net magnetization,[31–33] the AHE voltage is predominantly determined by the Co sublattice.[34,35] Our AHE measurements determine the $T_{\rm M}$ to be approximately 235 K. Around this temperature, the coercive field exhibits a significant enhancement [Fig. 1(c)], consistent with the behavior of conventional ferrimagnets.[36,37] As indicated from the AHE measurements in Fig. 1(b), when the temperature approaches $T_{\rm M}$, applying a strong external magnetic field along the easy axis drives the Co and Tb moments to deviate from their initial collinear alignment, as illustrated in Fig. 2. The criteria for the SC transition, shown in Fig. 2(b) through the anomalous Hall resistance R_{xy}, indicate that the transition occurs only under the application of a sufficiently large external field ($\boldsymbol{H}_{\rm ext} > 4$ T) near $T_{\rm M}$. Moreover, the critical field increases progressively as the temperature departs from the $T_{\rm M}$. We remark

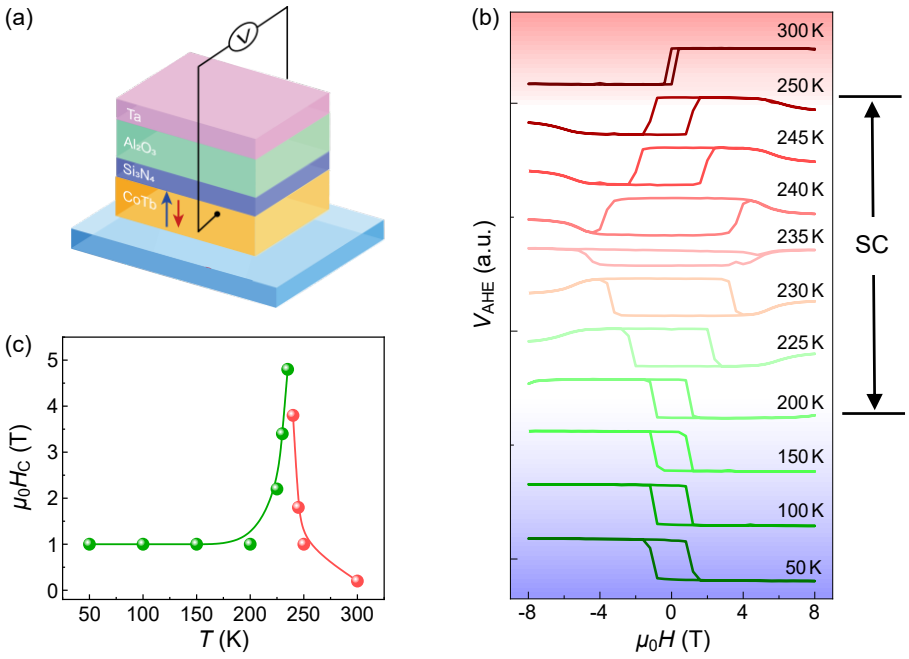

Fig. 1. (a) Schematic sketch of the experimental setup on the ferrimagnetic CoTb multilayer. Blue and red arrows denote the Co and Tb sublattice magnetic moments, respectively. (b) Out-of-plane AHE loops measured at different temperatures. (c) Temperature dependence of the CoTb coercivity $H_{\rm C}$.

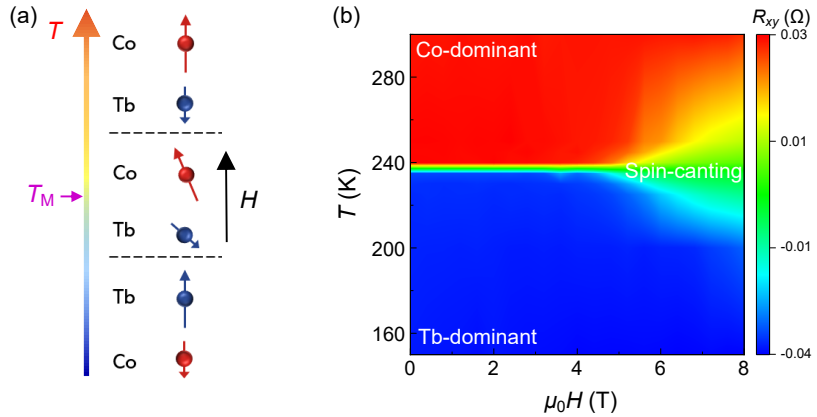

Fig. 2. (a) Schematic illustration of the magnetic moment orientations in the CoTb ferrimagnet at different temperatures under a strong out-of-plane external magnetic field. (b) Phase diagram of R_{xy} under different magnetic fields and temperatures.

that the SC state can be readily tuned by adjusting $T_{\rm M}$ and $K_{\rm eff}$. The composition ratio of the CoTb film controls its compensation temperature $T_{\rm M}$ as well as modifies the $K_{\rm eff}$. In some previous work, we have already successfully achieved a $T_{\rm M}$ that is close to room temperature.[38] The other way is to use Co/Tb multilayers with different thicknesses so that both the exchange coupling constant and $K_{\rm eff}$ can be tuned.

The devices used for measuring ANE are patterned using standard photolithography and a subsequent lift-off technique, as shown in Fig. 3(a). To generate thermal gradients in different directions, two heaters were employed. Heater 1 (30 nm Ta) was isolated from the CoTb layer by a 100 nm-thick Al_2O_3 layer deposited via Atomic Layer Deposition (ALD), enabling the application of an out-of-plane thermal gradient, $\nabla T_\perp$.[39] Heater 2 (30 nm Ta) was deposited directly on the substrate to provide an in-plane thermal gradient, $\nabla T_\parallel$. A cross-sectional schematic of the device is shown in Fig. 3(b). In Fig. 3(c), the ANE voltage along the y-axis, denoted as $V_{\rm ANE}$, follows the expected vector relationship, as confirmed by measurements under a 4 T rotating field at 300 K in the xy-, xz-, and yz-planes. It should be noted that the contribution of signals from the ordinary Nernst effect under an applied magnetic field is much smaller than that from ANE, and hence is not considered in the following analysis.[3] When rotating the magnetic field within the xy-plane, the magnetization $\boldsymbol{M}$ remains perpendicular to the thermal gradient ∇T,

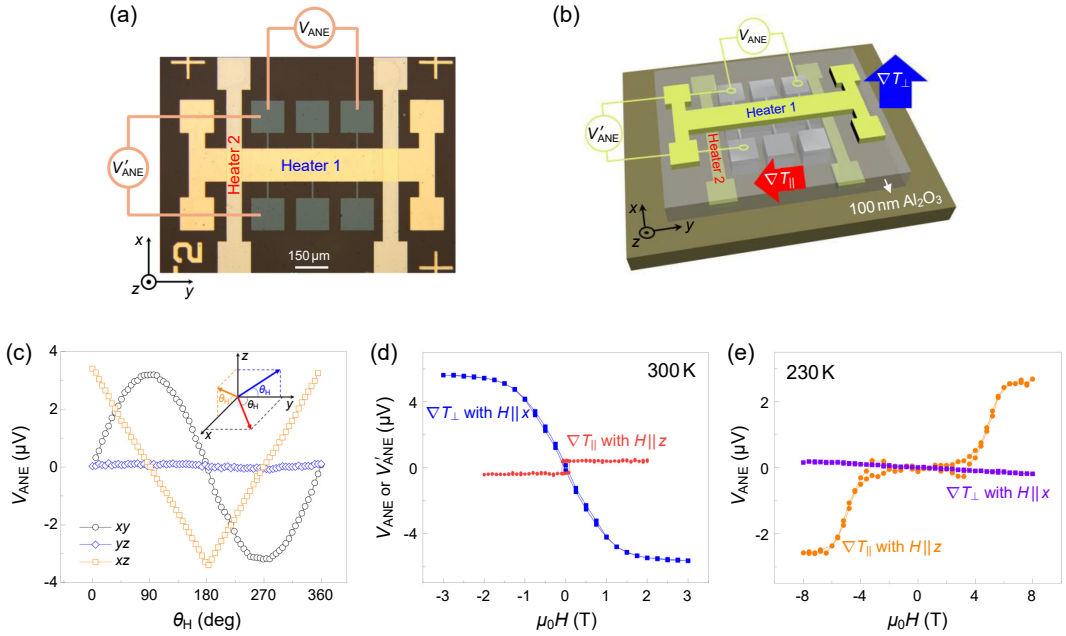

Fig. 3. (a) Optical image of the device and experimental setup for measuring ANE signals. The ANE voltage $V_{\rm ANE}$ is generated by the out-of-plane temperature gradient $\nabla T_\perp$ from Heater 1. The ANE voltage $V'_{\rm ANE}$ is generated by the in-plane temperature gradient $\nabla T_\parallel$ from Heater 2. (b) Cross-sectional schematic of the device and experimental setup for measuring ANE signals. (c) Angular dependence of $V_{\rm ANE}$ induced by $\nabla T_\perp$ under magnetic field rotation in the xy-, xz-, and yz-planes. (d) Comparison between $V_{\rm ANE}$ driven by $\nabla T_\perp$ under a magnetic field sweep along the x-axis and $V'_{\rm ANE}$ driven by $\nabla T_\parallel$ under a magnetic field sweep along the z-axis at 300 K. (e) Comparison of $V_{\rm ANE}$ under the same $\nabla T_\perp$ with magnetic field sweeps along the x- and z-axes at 230 K.

resulting in an ANE voltage component that varies with the rotation angle in the plane. Rotation in the yz-plane, however, produces a voltage solely along the x-axis. Under rotation in the xz-plane, the ANE response reflects not only the projection of $\boldsymbol{M}$ onto the field but also the pronounced PMA of the CoTb layer, which constrains $\boldsymbol{M}$ from fully tracking the external field and biases it toward the z-axis. As a result, the angular dependence of the ANE voltage in the xz-plane becomes significantly sharper than that in the xy-plane. Nevertheless, the magnitudes of the ANE are identical for rotations in the xy- and xz-planes, as long as the orthogonality condition between the magnetization $\boldsymbol{M}$ and the perpendicular temperature gradient $\nabla T_\perp$ is satisfied.

Next, we compared the ANE signals of $V_{\rm ANE}$ and $V'_{\rm ANE}$ from two standard configurations: the in-plane configuration ($\nabla T_\perp$ with $\boldsymbol{H} \parallel \hat{\boldsymbol{x}}$) and the out-of-plane configuration ($\nabla T_\parallel$ with $\boldsymbol{H} \parallel \hat{\boldsymbol{z}}$), respectively.[40] As shown in Fig. 3(d), under identical heating power, the $V_{\rm ANE}$ in the in-plane configuration (5.64 μV) far exceeds $V'_{\rm ANE}$ in the out-of-plane configuration (0.49 μV) at 300 K. This difference arises from a more effective temperature gradient $\nabla T_\perp$ being established within the Al_2O_3 intermediate layer. For real applications, a vertical thermal gradient can be easily created in highly compact arrays of devices, while the creation of a planar thermal gradient will inevitably occupy more space. Thus, we mainly focus on the $V_{\rm ANE}$ instead of $V'_{\rm ANE}$. However, $V'_{\rm ANE}$ can also be utilized for some other circumstances, such as planar thermoelectric applications and device quality checking, for example, once a broken device is present in the dense array of devices, a planar thermal gradient will be created and exerted on the neighboring devices, so that a $V'_{\rm ANE}$ signal is detectable. However, $V_{\rm ANE}$ becomes nearly negligible near $T_{\rm M}$ with the setup described above, as shown in Fig. 3(e). In contrast, a different scenario is observed when the applied field along $\hat{\boldsymbol{x}}$ is changed to along $\hat{\boldsymbol{z}}$: with increasing the applied magnetic field along the z-axis above 4 T, a rapid increase in $V_{\rm ANE}$ is observed, which further saturates around 6.5 T at a maximum value of 2.5 μV. This is directly associated with the SC state, which is observed in the above AHE measurements [Fig. 1(b)]: the application of a strong magnetic field along the z-axis induces the SC, causing $\boldsymbol{M}_{\rm Co}$ to cant toward the x-axis, thereby fulfilling the orthogonality condition between $\boldsymbol{M}$ and $\nabla T_\perp$, which is required for a sizable ANE.

To further verify the origin of SC-ANE, we systematically measured the $V_{\rm ANE}$ loops by sweeping the external magnetic field in the range from −8 T to 8 T at different temperatures. The magnetic field is applied along the z-direction with a 4° tilt toward the x-axis. Figure 4(a) shows the $V_{\rm ANE}$ generated by $\nabla T_\perp$ under a z-axis magnetic field at various temperatures. The magnitude of the anomalous Nernst voltage ($\Delta V_{\rm ANE}$) is quantified as $(V_{\rm ANE}^{\rm max} - V_{\rm ANE}^{\rm min})/2$. As shown in Fig. 4(b), $\Delta V_{\rm ANE}$ exhibits a strong temperature dependence, emerging only near $T_{\rm M}$ and increasing as the temperature approaches $T_{\rm M}$. This behavior closely follows the SC state diagram in Fig. 2(b), confirming that the ANE voltage is enhanced by the emergence of the SC state.

To explore the characteristics of the SC-ANE, we conducted simultaneous measurements of the AHE and SC-ANE. AC currents of different frequencies were applied to Heater 1 (I_1, ω_1) and through the CoTb film along the x-axis (I_2, ω_2). Two lock-in amplifiers are utilized to measure voltages along the y-axis. One lock-in amplifier is utilized to measure the first-harmonic Hall voltage generated by I_2, and the other is utilized to measure the second-harmonic ANE voltage generated by I_1. Since both measurements were performed under a magnetic field applied along the z-axis, this configuration enables the simultaneous detection of the AHE and ANE effects.

We focus on two representative temperatures below and above the magnetization compensation temperature $T_{\rm M}$, i.e., 225 K and 245 K, respectively. The applied magnetic field angle $\theta_{\rm H}$ within the xz-plane is varied through the measurements. The $V_{\rm AHE}$ and $V_{\rm ANE}$ signals share the same polarity and reverse together when increasing the temperature across $T_{\rm M}$, indicating that the ANE polarity in CoTb is determined mainly by the magnetization of the Co sublattice rather than the net magnetization.[41] The $V_{\rm AHE}$ is proportional to the z-component of $\boldsymbol{M}_{\rm Co}$,

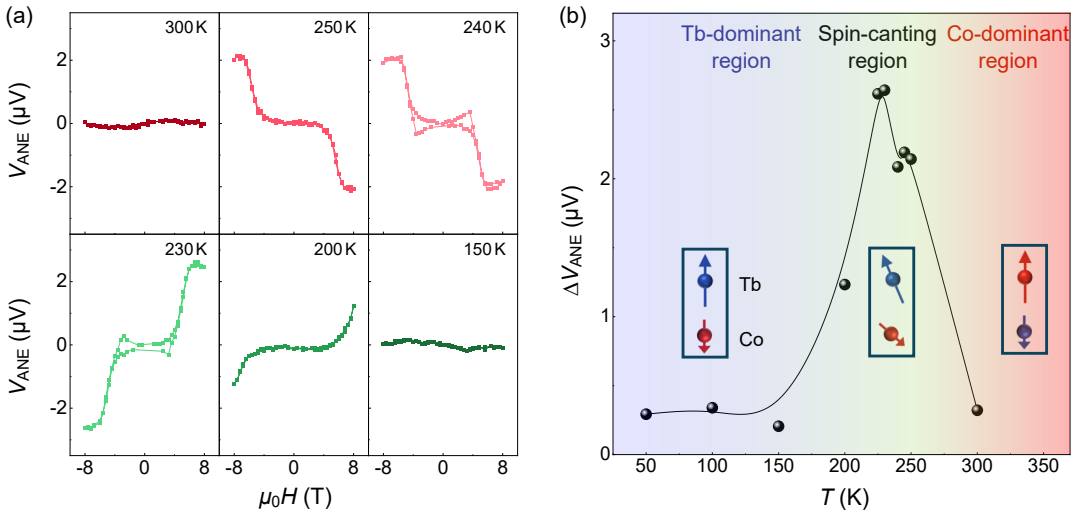

Fig. 4. (a) The ANE loops at different temperatures. (b) Temperature dependence of $\Delta V_{\rm ANE}$.

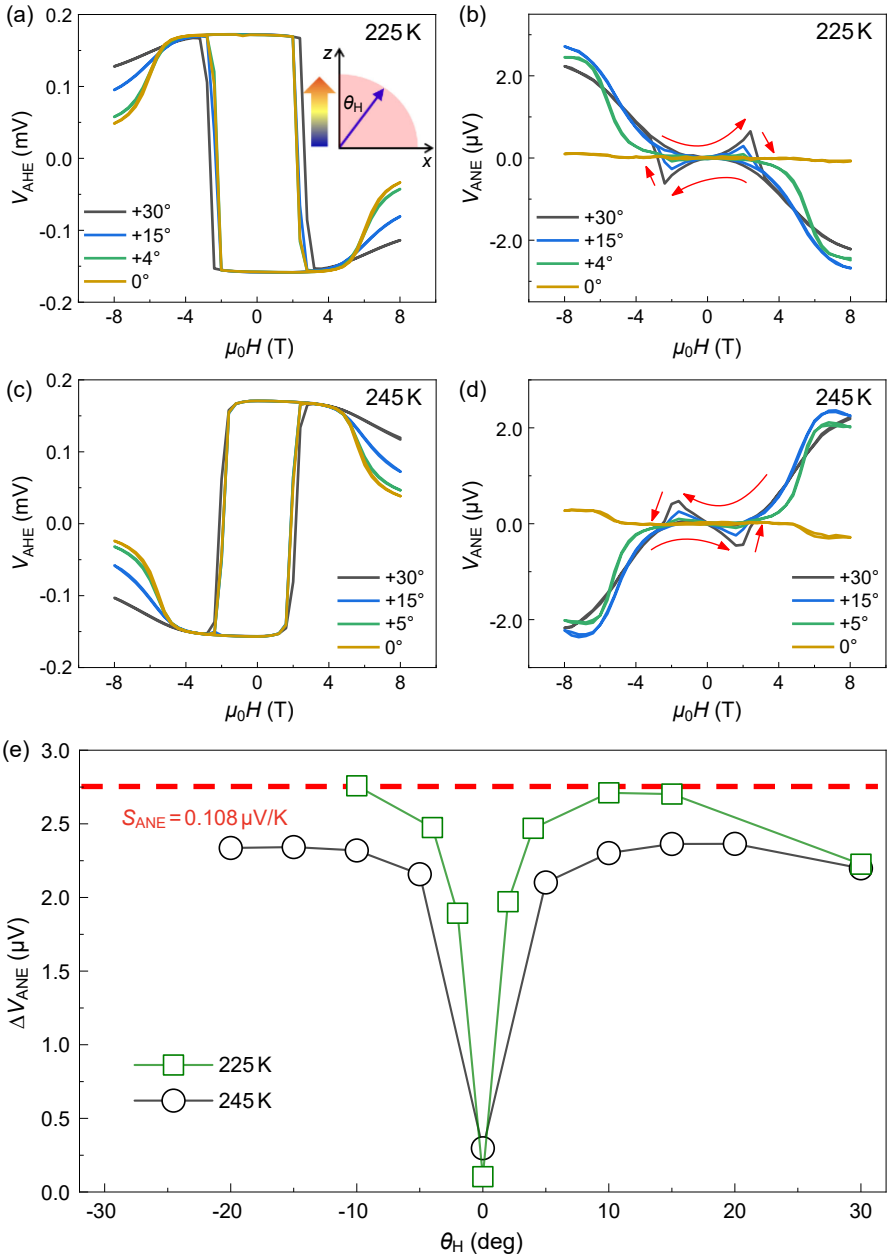

Fig. 5. (a) and (c) AHE, (b) and (d) ANE loops measured at different θ_H at 245 K and 225 K, respectively. (e) Angular dependence of ΔV_{ANE} at 225 K and 245 K.

while the V_{ANE} is governed by the x-component. As the external magnetic field $\boldsymbol{H}$ increases, particularly when it is applied along the z-axis ($\theta_H = 0°$), the V_{AHE} decreases at large magnetic fields, as shown in Figs. 5(a) and 5(c). This behavior again agrees with the fact that the magnetization is tilted away from the z-axis and into the SC state.

In contrast, the V_{ANE} exhibits a non-monotonic dependence on θ_H at both temperatures, as shown in Figs. 5(b) and 5(d). Although AHE measurements show that a z-axis magnetic field ($\theta_H = 0°$) induces the most significant SC, this same measurement geometry does not yield a pronounced ANE signal. However, as θ_H increases and the SC becomes less significant, ΔV_{ANE}, on the contrary, is well enhanced [Fig. 5(e)]. We attribute this behavior to the isotropic magnetic anisotropy within the film plane of CoTb. When the magnetic field is applied along the z-axis ($\theta_H = 0°$), a multi-domain state is present; the absence of a net in-plane magnetization component cannot generate a sizable V_{ANE}, since the tilted magnetic moment from the z-axis does not necessarily possess an x-component. As θ_H increases and the field tilts toward the x-axis, its growing x-component progressively aligns the magnetization, causing it to tilt accordingly and thereby enhancing the ANE voltage.

However, the above-mentioned scenario for effective generation of large ΔV_{ANE} can only happen when θ_H is small. This can be again explained by taking into account the energy terms that determine the magnetization orientations, as described in the free energy equation above. The further increase of θ_H will increase both the uniaxial anisotropy energy term and the exchange coupling energy term; thus, the SC state is no longer the lowest-energy

state, since the tilting of the magnetization from the z-axis is diminished and thereby reduces the ANE voltage. It is clearly shown in Fig. 5(e), where $\Delta V_{\rm ANE}$ decreases with further increasing $\theta_{\rm H}$ at both temperatures. Nevertheless, we can still determine the anomalous Nernst coefficient $S_{\rm ANE} = E_{\rm ANE}/\nabla T$, where $E_{\rm ANE} = \Delta V_{\rm ANE}/d$ and d denotes the separation between the voltage probes, which is 400 μm. Here, ∇T is calculated by comparing the longitudinal resistance (R_{xx}) of Heater 1 under the thermal gradient with its standard R_{xx} value at environmental temperature (T_1) to determine the device temperature (T_2). The thermal gradient is subsequently obtained by $\nabla T = \Delta T/t$, where $\Delta T = T_2 - T_1$ and t is the total thickness, including both the substrate and film stack thicknesses. At 225 K, ∇T is determined to be 0.07 K/μm. The largest $S_{\rm ANE}$ at 225 K is thus found to be 0.108 μV/K [see Fig. 5(e)], similar to the previously reported values for ferrimagnetic TM-RE alloy systems.[41,42]

The intriguing phenomenon of SC has recently been reported in various systems, enabling the observation of antiferromagnetic quantum AHE in $MnBi_2Te_4$ and giant spin-Seebeck effect in TbIG.[43,44] Here, SC facilitates the development of efficient micro/nano thermoelectric devices with PMA based on out-of-plane thermal gradients. Finally, it is noteworthy that the ANE can serve as a valuable complement to the AHE. In situations where the magnetic moment is confined primarily to the in-plane direction, rendering the AHE signal too weak for detection, the ANE can act as an effective and robust supplementary detection mechanism. This capability enhances the sensing performance of magneto-electronic devices. Furthermore, the linear response region of the ANE at high magnetic fields can be utilized for sensor applications.

In summary, we have demonstrated an SC-ANE in ferrimagnetic CoTb films, which can possibly offer an effective solution to the long-standing orthogonality conflict between PMA and an out-of-plane thermal gradient. Near the magnetic compensation temperature, the SC transition, induced by an applied magnetic field in the xz-plane with slight deviation from the z-axis, generates a significant in-plane magnetization component, enabling a large ANE coefficient up to 0.108 μV/K. Our systematic angular study reveals the unique characteristics of this effect and identifies the optimal measurement configuration. This work not only establishes the SC as a novel and powerful mechanism for controlling thermomagnetic conversion but also highlights ferrimagnetic alloys as a highly promising platform for developing high-stability, high-efficiency spintronic thermoelectric devices.

Acknowledgements. This work was supported by the National Key R&D Program of China (Grant No. 2022YFA1204002), Open Project Funding of the Key Laboratory of Intelligent Sensing System and Security (Ministry of Education), the International Science and Technology Cooperation Program under the 2023 Shanghai Action Plan for Science, Technology and Innovation (Grant No. 23520711200), the National Natural Science Foundation of China (Grant Nos. 52371246, 12274323, 52271188, 12174287, and 12374118), the Natural Science Foundation of Shanghai (Grant No. 23ZR1466800), and Open Fund of the State Key Laboratory of Spintronics Devices and Technologies (Grant No. SPL-2412).

References

[1] Bauer G E W, Saitoh E, and van Wees B J 2012 *Nat. Mater.* **11** 391
[2] Boona S R, Myers R C, and Heremans J P 2014 *Energy Environ. Sci.* **7** 885
[3] Uchida K 2021 *Proc. Jpn. Acad. Ser. B* **97** 69
[4] Cahaya A B, Tretiakov O A, and Bauer G E W 2015 *IEEE Trans. Magn.* **51** 0800414
[5] Yu H, Brechet S D, and Ansermet J P 2017 *Phys. Lett. A* **381** 825
[6] Qian Y T, Zhang J Y, Bi X Y, Chen P, Cao H Z, Xu W F, Liu Z Y, Zhai K, Yuan H T, and Huang J W 2025 *Chin. Phys. Lett.* **42** 090713
[7] Xiao D, Wang Y, Shi J, and Niu Q 2006 *Phys. Rev. Lett.* **97** 026603
[8] Nagaosa N, Sinova J, Onoda S, MacDonald A H, and Ong N P 2010 *Rev. Mod. Phys.* **82** 1539
[9] Shi Z, Xu S J, Ma L, Zhou S M, and Guo G Y 2020 *Phys. Rev. Appl.* **13** 054044
[10] Qin M S, Zhu P F, Ye X G, Xu W Z, Song Z H, Liang J, Liu K, and Liao Z M 2021 *Chin. Phys. Lett.* **38** 017301
[11] Uchida K I, Kikkawa T, Seki T, Oyake T, Shiomi J, Qiu Z, Takanashi K, and Saitoh E 2015 *Phys. Rev. B* **92** 094414
[12] Ramos R, Aguirre M H, Anadón A, Blasco J, Lucas I, Uchida K, Algarabel P A, Morellón L, Saitoh E, and Ibarra M R 2014 *Phys. Rev. B* **90** 054422
[13] Dieny B and Chshiev M 2017 *Rev. Mod. Phys.* **89** 025008
[14] Lee W L, Watauchi S, Miller V L, Cava R J, and Ong N P 2004 *Phys. Rev. Lett.* **93** 226601
[15] Fert A, Cros V, and Sampaio J 2013 *Nat. Nanotechnol.* **8** 152
[16] Heinze S, von Bergmann K, Menzel M, Brede J, Kubetzka A, Wiesendanger R, Bihlmayer G, and Blügel S 2011 *Nat. Phys.* **7** 713
[17] Zhang G, Luo Q, Wen X, Wu H, Yang L, Jin W, Li L, Zhang J, Zhang W, Shu H, and Chang H 2023 *Chin. Phys. Lett.* **40** 117501
[18] Garst M, Waizner J, and Grundler D 2017 *J. Phys. D: Appl. Phys.* **50** 293002
[19] Zhang H, Zhang Y, Hou Z, Qin M, Gao X, and Liu J 2023 *Mater. Futures* **2** 032201
[20] Hansen P, Clausen C, Much G, Rosenkranz M, and Witter K 1989 *J. Appl. Phys.* **66** 756
[21] González J A, Andrés J P and López Antón R 2021 *Sensors* **21** 5615
[22] Colino J, Andrés J P, Riveiro J M, Martínez J L, Prieto C, and Sacedón J L 1999 *Phys. Rev. B* **60** 6678
[23] Becker J, Tsukamoto A, Kirilyuk A, Maan J C, Rasing T, Christianen P C M, and Kimel A V 2017 *Phys. Rev. Lett.* **118** 117203
[24] Yang H, Huang J, Tian S, Xia K, Wang Z, Zhang Y, Ma J, Guo H, Zhang X, and Dai J 2025 *Chin. Phys. Lett.* **42** 080706
[25] Finley J and Liu L 2020 *Appl. Phys. Lett.* **116** 110501
[26] Kim S K, Beach G S D, Lee K J, Ono T, Rasing T, and Yang H 2022 *Nat. Mater.* **21** 24
[27] Hirata Y, Kim D H, Okuno T, Nishimura T, Kim D Y, Futakawa Y, Yoshikawa H, Tsukamoto A, Kim K J, Choe S B, and Ono T 2018 *Phys. Rev. B* **97** 220403
[28] Kittel C 2005 *Introduction to Solid State Physics* 8th Edition (Hoboken, NJ: Wiley)
[29] Bogdanov A N, Zhuravlev A V, and Rößler U K 2007 *Phys. Rev. B* **75** 094425

[30] Stark I, Stordeur M, and Syrowatka F 1993 *Thin Solid Films* **226** 185
[31] Mishra R, Yu J, Qiu X, Motapothula M, Venkatesan T, and Yang H 2017 *Phys. Rev. Lett.* **118** 167201
[32] Demirtas S, Camley R E, and Koymen A R 2005 *Appl. Phys. Lett.* **87** 202111
[33] Sala G, Lambert C H, Finizio S, Raposo V, Krizakova V, Krishnaswamy G, Weigand M, Raabe J, Rossell M D, Martinez E, and Gambardella P 2022 *Nat. Mater.* **21** 640
[34] Wang Y, Li C, Zhou H, Wang J, Chai G, and Jiang C 2021 *Appl. Phys. Lett.* **118** 071902
[35] Roschewsky N, Matsumura T, Cheema S, Hellman F, Kato T, Iwata S, and Salahuddin S 2016 *Appl. Phys. Lett.* **109** 112403
[36] Caretta L, Mann M, Büttner F, Ueda K, Pfau B, Günther C M, Hessing P, Churikoval A, Klose C, Schneider M, Engel D, Marcus C, Bono D, Bagschik K, Eisebitt S, and Beach G S D 2018 *Nat. Nanotechnol.* **13** 1154
[37] Gao S, Zheng Y, He S, Fang H, and Zhang Y 2025 *Chin. Phys. Lett.* **42** 070701
[38] Zhu W, Tang M, Pan C, Xie N, Li Y, Xu A, Zhang J, Fan W, Shi Z, and Zhai K 2025 *Adv. Funct. Mater.* 2505415
[39] Cappella A, Battaglia J L, Schick V, Kusiak A, Lamperti A, Wiemer C, and Hay B 2013 *Adv. Eng. Mater.* **15** 1046
[40] Elahi E, Al-Kahtani A A, Dastgeer G, Aftab S, Aziz J, Iqbal M W, Manzoor M, Jeong J, Suleman M, Ahmed B, Koyyada G, and Sharma P R 2023 *Appl. Mater. Today* **32** 101846
[41] Liu R, Cai L, Xu T, Liu J, Cheng Y, and Jiang W 2023 *Appl. Phys. Lett.* **122** 022406
[42] Odagiri M, Imaeda H, Yagmur A, Kurokawa Y, Sumi S, Awano H, and Tanabe K 2024 *Appl. Phys. Lett.* **124** 142403
[43] Lian Z, Wang Y, Wang Y, Dong W H, Feng Y, Dong Z, Ma M, Yang S, Xu L, Li Y, Fu B, Li Y, Jiang W, Xu Y, Liu C, Zhang J, and Wang Y 2025 *Nature* **641** 70
[44] Li Y, Duan Y, Wang M, Lang L, Zhang Y, Yang M, Li J, Fan W, Shen K, Shi Z, and Zhou S M 2024 *Phys. Rev. Lett.* **132** 056702